Iranian Journal of Chemical Engineering

Journal Homepage: www.ijche.com

pISSN: 1735-5397
eISSN: 2008-2355

Regular Article

Impact of the Static Bed Height on the Minimum Spouting Velocity of Polydispersed Agglomerates in a Conical Fluidized Bed

A. R. Bahramian *

Department of Chemical Engineering, Hamedan University of Technology, P. O. Box: 65155, Hamedan, Iran

ARTICLE INFO

Article history:
Received: 2022-09-28
Accepted: 2023-01-28
Available online: 2023-01-29

Keywords:
Fluidization,
Bed Loading,
Particle Size Distribution,
Interparticle Force,
CFD-DEM Modeling,
Conical Fluidized Bed

ABSTRACT

The effect of static bed height on the minimum spouting velocity (u_{ms}) of polydispersed TiO_2 agglomerates was studied experimentally and numerically in a conical fluidized bed. The experiments were carried out at different static bed heights with Gaussian and narrow-cut particle size distribution (PSD) through fluidization and defluidization stages. The bed consisted of simple-agglomerates with the sizes of 30-90 µm belonging to the Geldarts' group A classification .The effect of PSD and interparticle force (IPF) on the predicted u_{ms} of the bed and hysteresis in the bed pressure drop were studied by an approach having coupled computational fluid dynamics and discrete element method (CFD-DEM). The experimental data showed that chosing a bed with Gaussian-type PSD led to more accurately predicting u_{ms} than when chosing one with the narrow-cut type PSD. The simulation results showed that the impact of IPF became more critical than that of the PSD type, because of an increase in static bed heights on the expected u_{ms}. The least discrepancy between the experimental data and simulation outputs was obtained in the bed with Gaussian-type PSD and low static bed heights, which confirmed the accuracy of simulation results. The results showed that the PSD-type and IPF led to a change in the type of the flow regime in the conical fluidized bed. The results showed that the bed with narrow-cut type PSD had a hydrodynamic behavior similar to that of spouting and slugging regimes, while the fluidization quality of the bed improved by the existence of fine particles.

DOI: 10.22034/ijche.2023.363885.1458 URL: https://www.ijche.com/article_165982.html

1. Introduction

Conical fluidized beds, which are mainly used for the fluidization of sticky and coarse particles with a wide particle size distribution (PSD), have the exclusive hydrodynamic characteristics of both conventional fluidized

*Corresponding author: bahramian@hut.ac.ir (A. R. Bahramian)

beds and spouted beds [1-3]. The hydrodynamic behavior of a conical fluidized bed mainly depends on the properties of particles, such as their density, size and classification type in Geldart's chart, and the characteristics of the bed type, such as the ratio of the diameter of the inlet in the vessel to the diameter of particles, the ratio of the height of the cone to the height of the cylinder, and the angle of the cone [4, 5]. The particles' motions in a conical fluidized bed are categorized into those of three regions just similar to the classification of the bed zones in a spouted bed. A spout zone is located at the core of the bed; and an annular zone is located in the area between the spout and the bed walls. The fountain zone mainly forms in the conical/cylindrical interface of the fluidized bed.

In the past decades, many experiments have been focused on the study of the fluidization characteristics of conical fluidized beds, such as the minimum spouting velocity u_{ms}, static bed height h_0, and bed expansion ratio h/h_0, where h and h_0 are the heights of the expanded bed and the static bed respectively [6, 7]. A change in particle size, due to the presence of interparticle forces (IPFs), leads to the formation of nanoparticle (NP) agglomerates during fluidization, which can be used to determine the hydrodynamic behavior of the bed [8, 9]. NP agglomerates are undesirable materials that cause fundamental challenges in many industries such as food drying, pharmaceuticals, powder production, and nanomaterial production industries [9-11]. The formation of NP agglomerates occurs through primary NPs binding to one another and the formation of simple-agglomerates [12], which are mainly between 20 and 100 μm in size [12, 13]. The effect of IPF on the hydrodynamic behavior of fine powders is particularly significant in humid environments [8]. Castellanos et al. [13] found that the van der Waals force has a significant effect on the flow transitional regime from group C (cohesive) to group A (aeratable) and from group A to group B (bubbling) behaviors. The contribution of IFPs, gravitational and inertial forces can affect the hydrodynamic behavior of the bed [9]. The effect of static bed height on the fluidization behavior of the conventional fluidized bed has been widely studied in literatures [14]. It has been shown that by increasing h_0, the values of u_{mf} increase, while h/h_0 decreases.

The relationship between u_{mf} and h_0 is a function of other hydrodynamic parameters such as the size, density and porosity of particles as well as PSD [15]. Liu et al. [10] revealed the low impact of h_0 on the u_{mf} of the bed containing microparticles (MPs) with different PSDs. Rao et al. [16] found that the effect of h_0 on u_{mf} in a fluidized bed containing MPs is practical and depends on the diameter of the column. Liu et al. [17] showed that the probability of pressure overshoot becomes high in the case of Geldart's B particles. Shabanian et al. [18] showed that the degree of pressure overshoot in the fluidization characteristics curve increases by increasing IPFs, which is also accompanied by the increment of u_{mf}.

Extensive research on conical fluidized beds has led to the conclusion that PSD has a significant effect on u_{ms}, where its value decreases in the bed with wide PSD and its value vary depending on the mass fraction of particles with different sizes due to different types of IPF [19]. The hydrodynamic behavior of the beds with different PSDs, including uniform, narrow-cut, Gaussian, non-normal, binary mixture, and flat (wide) types of powders have been investigated in literatures

[20]. Gauthier et al. [21] pointed out that the PSD types of Gaussian and narrow-cut exhibited a similar u_{mf}, while the binary and uniform-types of PSD showed various fluidization behaviors in the conventional fluidized bed. Due to the complexity of the simultaneously studying PSD and IPFs, their effetc on the fluidization of NPs in the conical fluidized bed requires more attention to this issue.

Numerical modeling by computational fluid dynamics (CFD) approach coupled with the discrete element method (DEM) has been reported to study the hydrodynamic characteristics of the fluidized beds [22-25]. Recent studies are devoted to the particles mixing in the bed, the tendency of NPs to form agglomerates, as well as the mechanism of agglomeration or breakage during the fluidization of NPs [17, 26]. The CFD-DEM modeling results revealed that IPF would hinder the beginning of the spouting and fluidization state. An increase in the cohesive forces of the fine powder leads to the formation of simple-agglomerates. Thus, higher gas velocities are needed to overcome the bed resistance against fluidization. [17, 27, 28]. Xu et al. [24] showed that the difference between the bed pressure drop and maximum bed pressure drop increased by increasing h_0 in the case of Geldart's B MPs [24]. Bahramian and Olazar [19] found the interaction between the TiO_2 agglomerates by combining Mindlin-Dersiewicz and Johnson-Kendall-Roberts (JKR) contact models in a conical fluidized bed. There was good agreement between the results of the particle velocity profiles in the spout zone and those of the annular zone by choosing the friction coefficient close to one, which considers the nearly elastic collisions between the particles. Earlier, Bahramian et al. [29] found that the free-slip boundary condition (BC) in the CFD modeling of TiO_2 MPs led to a reasonable agreement between the experimental data and simulation results. They also showed that the most significant dissipation rate of the gas-solid flow was because of the existence of drag force between the gas and particles.

According to the author's knowledge, the effects of IPF and PSD on the fluidization characteristics of TiO_2 simple-agglomerates in a conical fluidized bed with different static bed heights have not been investigated so far. Also, no CFD-DEM simulation was caried out to study the simultaneous impact of the mentioned parameters on the prediction of the u_{ms} of the conical fluidized bed. This study aims to understand the effect of the initial static bed height on the fluidization behavior of polydisperse TiO_2 simple-agglomerates in a lab-scale conical fluidized bed. The pressure drop profiles were determined to study the effect of IPF, and the PSD-type of the bed on the predicted u_{ms} which was studied numerically using the CFD-DEM approach during fluidization and defluidization stages. Two particulate systems, including the Gaussian-type, and narrow-cut type PSD were examined in the simulations to evaluate the simulation results with the experimental data. The relative error analysis was used to investigate each of the mentioned parameters at different static bed heights to predict u_{ms} values.

2. Experimental section

The fluidization behavior of TiO_2 NPs with the primary size of 23 ± 3 nm was studied in a conical fluidized bed. The physical properties of the primary TiO_2 NPs and resulted simple-agglomerates belonging to the Geldarts' group A classification are shown in Table 1. The size distribution of simple-agglomerates was

determined by a PSD analyzer (Partica LA-960, HORIBA, Ltd.).

Figure 1 shows the schematic image of the system (Figure 1a), where the diameters of the inlet and outlet in the vessel were 0.06 and 0.12 m respectively (Figure 1b). The values of h_0 were set to 1.2, 2.4, 3.6, and 4.8 cm. TiO_2 NPs was fluidized in the bed equipped with a 200 mesh screen at the bottom as the gas distributor. Two pressure meters, one just above the gas distributor and the other on the top of the bed, were provided to record the total bed pressure drop. Fluidization experiments were performed in the bed from the fixed state to the full fluidization condition by increasing the inlet gas velocity, u_g, from 0 to 0.7 m/s, and then decreasing the gas velocity until the bed reached the initial state. The fluidization characteristic curves were plotted to determine u_{ms} for different h_0 values. All fluidization experiments were performed at atmospheric pressure and ambient temperature (300 K). Additional details can be found in the literature [12, 14].

Table 1
The physical properties of the primary TiO_2 NPs and resulted simple-agglomerates.

Property	Value (average value)	
Primary NPs (d_p, nm)	23 ± 3	
Simple-agglomerates size (μm)	30-90	
Particle density (ρ_p, kg/m^3)	1530-1900	
Bulk density (ρ_b, kg/m^3)	h_0 (cm)	ρ_a (kg/m^3)
	1.2	233
	2.4	230
	3.6	226
	4.8	223
Maximum packing limit ($\alpha_{agg,\,max}$)	h_0 (cm)	$\alpha_{agg,\,max}$ (-)
	1.2	0.75
	2.4	0.76
	3.6	0.77
	4.8	0.79

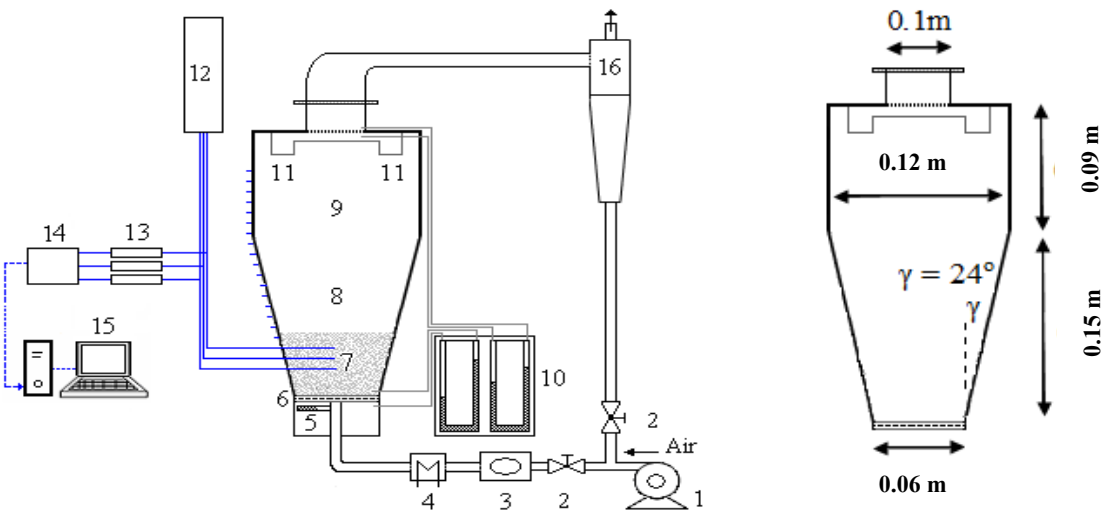

(a) (b)

1. Air compressor, 2. Valves, 3. Rotameter, 4. Electrical clement, 5. Probe thermometer, 6. Gas distributor, 7. Materials bed, 8. Conical section, 9. Cylindrical section, 10. Manometers, 11. Bag filters, 12. Light source, 13. Detectors, 14. Amplifier, 15. Computer and monitoring

Figure 1. (a)The schematic image of the system, (b) the dimensions of the bed.

3. CFD-DEM modeling

3.1. Governing equations

The adhesive CFD-DEM model was used in the simulations to study the hydrodynamic behavior of the simple-agglomerates in the conical fluidized bed. The governing equations based on gas and solid phases were analyzed by local averaged Navier-Stokes equations which are shown in Table 2 and Table 3 respectively. The momentum transfer between the gas and particle phase is determined by the "drag force scale factor" ξ (Table 2). The input value of ξ was selected in the range of 0.2-0.3, as reported by McKeen and Pugsley [30]. In the traditional DEM approach, the linear and angular velocities of each particle are tracked by the Lagrangian approach. The governing equations for the solid phase were determined by the motion of fluidized agglomerates according to Newton's equation. Hamaker constant, H, which depends on the material's properties, lies in the range of 10-19-10-20 J [31]. A minimum cutoff distance (hmin) is used to avoid the vdW force approaching infinity as the separation distance approaches zero.

Table 2

The governing equations for the gas phase obtained by local averaged Navier-Stokes equations.

Mass and momentum conservation equations:	
$\frac{\partial}{\partial t}(\varepsilon_g \rho_g) + \frac{\partial(\varepsilon_g \rho_g u_g)}{\partial x_i} = 0$	(1)
$\frac{\partial}{\partial t}(\varepsilon_g \rho_g u_g) + \nabla \cdot (\varepsilon_g \rho_g u_g u_g) = -\varepsilon_g \nabla P_g + \varepsilon_g \rho_g g + S_P - \nabla \cdot (\varepsilon_g \tau_g)$	(2)
Volume fraction of gas:	
$\varepsilon_g = 1 - \frac{\sum_{i=1}^{n_p} V_i}{V_{cell}}$	(3)
Momentum transfer between the gas and particle phases:	
$S_P = -\frac{1}{V_{cell}} \sum_{i=1}^{n_p} f_{d,i}\, \xi$	(4)
Drag force between gas and particles:	
$f_{d,i} = \frac{v_{p,i} \beta_i}{(1-\varepsilon_g)}(u_g - v_p)$	(5)
Gidaspow drag function:	
$\beta_i = \begin{cases} 150 \frac{\varepsilon_p (1-\varepsilon_g)\mu_g}{\varepsilon_g (\phi_p d_p)^2} + 1.75 \frac{\varepsilon_p \rho_g \lvert v_p - u_g \rvert}{\emptyset_p d_p} & \varepsilon_g < 0.8 \\ \frac{3}{4} C_{D,i} \frac{\varepsilon_p \rho_p}{d_p} \lvert v_p - u_g \rvert \varepsilon_g^{-2.65} & \varepsilon_g \geq 0.8 \end{cases}$	(6)
Gas-solid interphase drag function coefficient:	
$C_{D,i} = \begin{cases} \frac{24}{Re_p \varepsilon_g}(1 + 0.15 (Re_p \varepsilon_g)^{0.687} & Re_p \varepsilon_g < 1000 \\ 0.44 & Re_p \varepsilon_g \geq 1000 \end{cases}$	(7)
$Re_i = \frac{\rho_g \lvert v_p - u_g \rvert \, \phi_i d_i}{\mu_g}$	(8)

Viscous stress tensor in the momentum equation: $\boldsymbol{\tau}_g = \mu_g[(\nabla \mathbf{u}_g) + (\nabla \mathbf{u}_g)^T - \frac{2}{3}(\nabla \mathbf{u}_g)\mathbf{I}]$	(9)

Table 3

The governing equations and sub-models of the CFD-DEM simulation for the solid phase obtained by local averaged Navier-Stokes equations.

Motion equation of particle: $\mathbf{m}_i \frac{d\mathbf{v}_i}{dt} = \mathbf{f}_{p,i} + \mathbf{f}_{vdw} + \mathbf{f}_{c,i} + \mathbf{f}_{d,i}\xi + \mathbf{m}_p\,\mathbf{g}$	(1)
$\mathbf{I}_i \frac{d\omega_i}{dt} = \mathbf{T}_i$	(2)
Torques acting on the particle: $\mathbf{T}_i = \sum_{j \in \text{contact list}} (\mathbf{R}_i\,\mathbf{n}_{ij} \times \mathbf{f}_{t,ij})$	(3)
Pressure gradient force exerting on the agglomerate: $\mathbf{f}_{p,i} = -\nabla \mathbf{P}_g(\mathbf{x}_i)\,\mathbf{V}_i$	(4)
Van der Waals force arising from particle-particle: $\mathbf{f}_{vdw,i-j} = \frac{\mathbf{HR}}{12\,\mathbf{h}_{i-j}^2}$	(5)
Waals force arising from particle-wall interactions: $\mathbf{f}_{vdw,i-w} = \frac{\mathbf{HR}}{6\,\mathbf{h}_{i-w}^2}$	(6)
Contact force on an agglomerate: $\mathbf{f}_{c,i} = \sum_{j \epsilon \text{ contact list}} (\mathbf{f}_{n,ij} + \mathbf{f}_{t,ij})$	(7)
Normal component of the contact force: $\mathbf{f}_{ij}^n = -(\mathbf{k}_n\boldsymbol{\delta}_n + \boldsymbol{\eta}_n\mathbf{v}_{n,ij})\mathbf{n}$	(8)
Relative velocity of particles: $\mathbf{v}_{ij} = (\mathbf{v}_i - \mathbf{v}_j) + (\mathbf{R}_i\boldsymbol{\omega}_i + \mathbf{R}_j\boldsymbol{\omega}_j) \times \mathbf{n}_{ij}$	(9)
Tangential component of the contact force: $\mathbf{f}_{t,ij} = \begin{cases} -(\mathbf{k}_t\boldsymbol{\delta}_t\mathbf{t}_{ij} + \boldsymbol{\eta}_t\mathbf{v}_{t,ij}) & \text{for } \lvert\mathbf{f}_{t,ij}\rvert \le \mu_f\lvert\mathbf{f}_{n,ij}\rvert \\ -\mu_f\lvert\mathbf{f}_{n,ij}\rvert\,\mathbf{t}_{ij} & \text{for } \lvert\mathbf{f}_{t,ij}\rvert > \mu_f\lvert\mathbf{f}_{n,ij}\rvert \end{cases}$	(10)
Tangential relative velocity: $\mathbf{v}_{t,ij} = \mathbf{v}_{ij} - \mathbf{v}_{n,ij}$	(11)
Tangential unit vector: $\mathbf{t}_{ij} = \frac{\mathbf{v}_{t,ij}}{\lvert\mathbf{v}_{t,ij}\rvert}$	(12)

The granular Bond number Bog, which is defined as the ratio of fvdw to the weight force, was used to quantify the cohesive nature of the simple-agglomerate [32]. fvdw was selected in the range of 0.4-4.0 nN that was proposed for Geldart A particles [33-34], thus the values of

Bog lie in the range of 5-50. The value of ξ which is estimated by varying Bog number is shown in Figure 2. As shown, the values of ξ were 0.3 and 0.2, estimated for Bovdw of 5 and 50 respectively. This result agreed with the actual condition, where the umf increases by increasing the cohesive forces between simple-agglomerates.

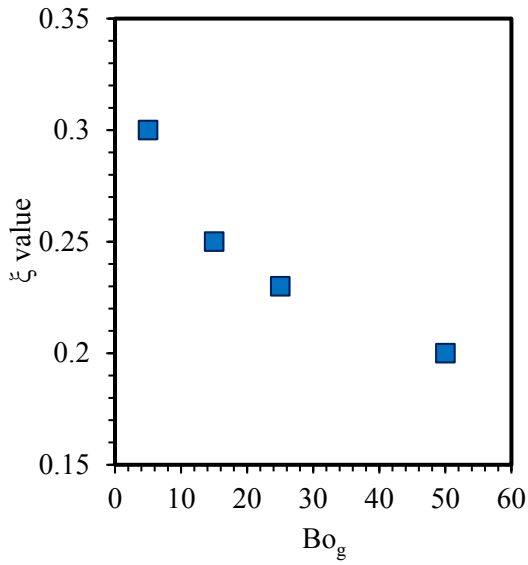

Figure 2. The computational analysis for the value of ξ estimated by changingn the Bo_g number.

3.2. Adhesive CFD-DEM model

The standard CFD-DEM model, an adhesive contact model, was used for the prediction of the NP agglomerate fluidization. A more detailed description of CFD-DEM models can be found in literatures [30-34]. The adhesive forces are due to particle-particle and wall-particle interactions and are calculated by the adhesive contact model. The interaction forces between NP agglomerates were modeled by the inelastic Hertzian model (HM), including the combination of the Mindlin-Dersiewicz model and the JKR (Johnson-Kendall-Roberts) contact model, where the maximum interactions between the NPs were expected because of Coulomb friction [32]. The non-linear elastic contact force models including HM and JKR models are introduced in Table 4. The contact force from particle-particle and particle-wall collisions of aeratable powders was described by a soft-sphere model [35-37]. The models' capability to capture the collisional behavior depends upon the force-displacement ($\mathbf{F}_{n,ab}$-δ_{ab}) relationship. Atomic force microscopy-based nanoindentation analysis showed that TiO_2 NPs were adhesive, and behaved like elastic-plastic materials [12].

Table 4

The non-linear elastic contact models used in the study.

Contact model	Component	Basis	Formula
Hertz-Mindlin theory	Normal	Hertz theory	$\mathbf{F}_n = -4/3\ \mathbf{E}_{eq}\sqrt{R_{eq}\cdot\delta_n^{3/2}}$
	Tangential	Mindlin & Deresiewicz theory	$\mathbf{F}_t = 8\mathbf{G}_{eq}\sqrt{R_{eq}\cdot\delta_n\cdot\delta_t}$
Hertz-Mindlin + JKR model	-	Surface energy	$\mathbf{F}_{JKR} = \frac{4E_{eq}a^3}{3R_{eq}} - \sqrt{8\pi a^3\Delta\gamma E_{eq}}$

3.3. Simulation procedure and conditions

The simulation procedure was based on the following steps:

Step 1: A polydispersed bed was generated inside the conical part of the vessel and settled under gravity to form packed beds with h_0 values corresponding to 1.2, 2.4, 3.6, and 4.8 cm. Simulations were performed with similar h_0. The total number of agglomerates for the beds with h_0 values of 1.2, 2.4, 3.6, and 4.8 cm, were 2.5961×10^7, 3.8942×10^7, 5.8413×10^7, and 8.7619×10^7 respectively. The density of

simple-agglomerates was set at 2430 kg/m^3, while the shape factor of particles was set at 0.82.

Step 2: First, the bed was fluidized by gas (airflow) to attain a steady-state condition in the bed, and then the bed was defluidized to reach a fixed-bed state by decreasing the gas (airflow) to zero to obtain the pressure drop profile. The near-wall approach was used to attain a solution for mesh independency.

The boundary conditions (BCs) used in the simulations included:

(1) The uniform gas (airflow) was specified at the inlet, while the outflow BCs with zero velocity gradients were assumed for each phase along the axial direction at the outlet.

(2) At the walls, the no-slip BC was used for the gas phase. At the same time, the BC developed by Johnson and Jackson was applied for the tangential velocity of the solid phase.

(3) The pressure was considered to be the same as of the atmospheric condition.

(4) The interaction between the solids and wall was regarded as a noncohesive collision, thus the value of $\mathbf{f_{vdw,i-w}}$ (Eq. 6 in Table 3) was considered to be zero.

Step 3: the simulation runs were performed on a two-dimensional axisymmetric geometry using an EDEM 2.6 simulator and the results were recorded for being analyzed. The time steps in the CFD simulations varied from 5 × 10^{-5} to 1 × 10^{-3} s, while in the DEM simulations they were in the time interval of ~ 1-2 × 10^{-7} s. The CFD-DEM simulations were performed on a PC with four processing cores exploiting the MPI parallel solver of Ansys Fluent 19.2. The total time necessary to simulate 3.0 s from the bed was about 72 hours. Other information required for the simulation is given in Table 5.

Table 5

The parameters used in the CFD-DEM simulations.

Property (symbol, unit)	Value	Property(symbol, unit)	Value
Agglomerates diameter (d_p, μm)	30-90	Normal spring constant (k_n, N/m)	700
Mean agglomerate density ($\rho_{p,avg}$ kg/m^3)	1730	Normal restitution coefficient (e_{ss})	0.95
Young modulus (E , kPa)	1.3 × 10^5	Friction coefficient (μ)	0.1
Hamaker constant (H, J)	1.2 × 10^{-19}	Minimum cutoff distance (h_{min}, nm)	0.5
Poisson' ratio (σ)	0.33	Maximum cutoff distance (h_{max}, μm)	15
Gas pressure (P_g, Pa)	1013251.	cell size (δ, mm)	1.2-2.2

Two different PSD-types, including Gaussian and narrow-cut, which were obtained based on the weight fraction of the simple-agglomerates, are shown in Figure 3. In the Gaussian-type PSD, the weight fractions of simple-agglomerates were in the range of 1.0 to 42.0 wt %, while in the narrow-cut type PSD the weight fractions of simple-agglomerates were in the range of 0.5 to 57.0 wt %. The sauter mean diameter of agglomerates was fixed and equal to 58 μm in all simulations, which was an approximation of the same of the PSD analysis.

3.4. Meshing strategy and grid-sensitivity analysis

A typical computational meshing strategy with a rectangular grid and a uniform structure was used in the simulations, which is shown in Figure 4. The computational domain was

discretized into 46000 grid cells. The sizes of grids were determined to be 1.2 mm and 2.2 mm in the axial and radial directions respectively. Furthermore, the near-wall refinement in the range of 0.4-0.5 r/R was used. This meshing strategy was selected to fulfill the conditions for the use of the near-wall model and achieve a solution that is independent of the mesh density.

The grid-sensitivity analysis was done to ensure that accurate numerical results were obtained in this study. Table 6 shows the simulation results of the grid independence analysis to determine u_{ms} values. The computational domains were discretized using 11500, 23000, 34500, 46000, and 53500 grid cells. The computational mesh was refined until an acceptable error between two consecutive meshes was achieved to predict the u_{ms} value. An analysis of variance was performed to determine whether the predictions were independent of the grid cell number. It is seen that the relative error in the predicted minimum spouting velocity is below 1.0 % by increasing the mesh number to 46000. Thus, considering the computational cost and accuracy, the mesh with 46000 grid cells was applied for further simulations.

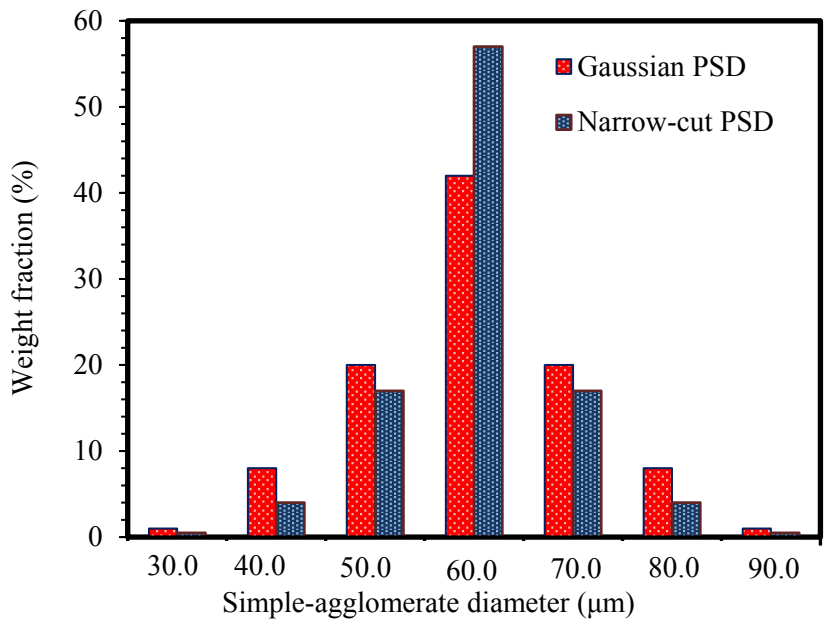

Figure 3. The PSD types of simple-agglomerates considered in the simulations.

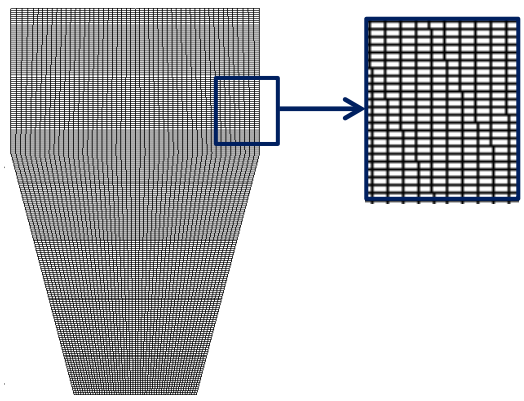

Figure 4. The computational mesh strategy and rectangular grid used in the simulations.

Table 6

The grid independency analysis to predict u_{ms} values.

Grid No.	Relative errors between two consecutive grids (%)	Simulation time of optimized grid (h)
11,500	16.76	~46
23,000	13.33	~51
34,500	9.65	~59
46,000	6.51	~67
53,500	5.86	~76

4. Results and discussion

4.1. Experimental data

Figure 5 shows the experimental data of normalized pressure drop profiles of the bed with h_0 values of 1.2, 2.4, 3.6, and 4.8 cm. The results are presented in fluidization curve (a), and defluidization curve (b). The normalized pressure drop increases gradually by increasing u_g to its maximum value corresponding to u_{ms}, where pressure drop approximately balances the weight of particles per unit area. After this point, the bed pressure drop reaches above the weight of particles per unit area, which has been called overpressure [1, 12, 17]. Finally, the bed pressure drop decreased gradually and fluctuated around a constant value. The experimental results suggested that the bed did not reach its maximum random packing before attaining the fluidization stage (Figure 5a). In contrast, the defluidization curve follows the initial fluidization at $1.1u_{ms}$, which is called pressure overshoot phenomena (Figure 5b). At $u_g = 1.1u_{ms}$, the bubbling flow regime is observed, which is indicated by u_{mb}. The coexistence of particle-particle cohesive forces led to difficulties in characterizing the reason for the pressure overshoot and hysteresis phenomena before the fluidization of Geldart A particles [38].

The defluidization curves are smoother than the fluidization ones in the bed pressure drop profile (Figure 5b). The hysteresis behavior in the fluidization and defluidization pressure drop curves becomes more prominent by increasing h_0, which is associated with more contacts between the particles. An increase in the h_0 value led to an increase in the cohesion force of the particles and the particle-wall interactions. By expanding the bed depth, more airflow was necessary to fluidize interlocking particles, which led to an increase in the bed pressure drop and an increase in the u_{ms} values. However, the results showed that the relationship between u_{ms} and h_0 is to follow a gradual curve with a decreasing pattern.

The sieve test showed that the weight fraction of particles in the bed tends to form the Gaussian-type PSD. Also, the polydispersity of particles is increased by increasing the static bed height. On the other hand, the error analysis results showed that by increasing the static bed height, the uncertainty of the results increased. Previous results showed that the substitution of particles with high cohesive force instead of particles with lower adhesion force led to shifting the Geldart's classification from group A to C and changes in the flow regime of the bed [39].

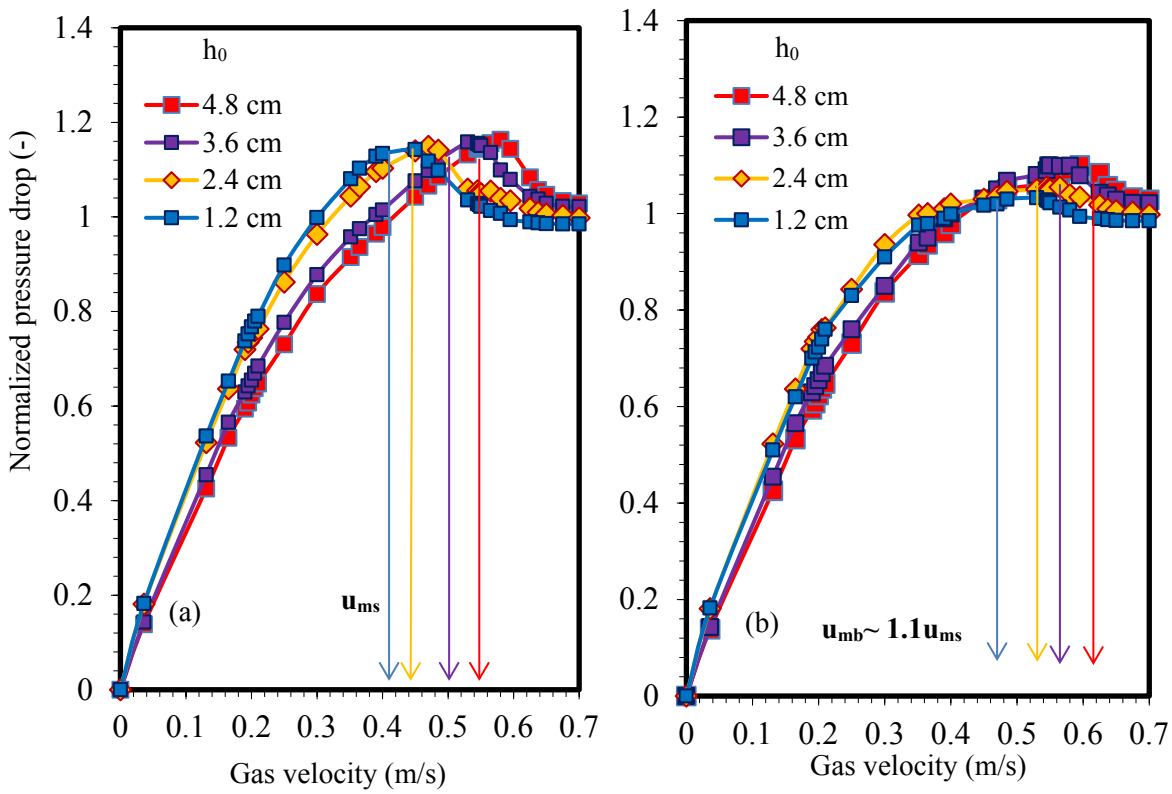

Figure 5. The experimental data of the normalized pressure drop pro files of the bed with h_0 values of 1.2, 2.4, 3.6, and 4.8 cm [(a) fluidization, and (b) defluidization curves].

4.2. Simulation results

4.2.1. Effect of IPF

Figure 6 shows the contour plots of the solid volume fraction of the fluidization (top images) and defluidization (bottom images) cycles for the simulated bed at the $u_g = 0.6$ m/s and h_0 = 4.8 cm by applying different $\mathbf{Bo_g}$ values of 5, 15, 25, and 50. The solid volume fraction contours showed that the size and number of the bubbles increased, and at the same time, the spouting condition of particles decreased by increasing $\mathbf{Bo_g}$. This result revealed that the fluidization of the particles was postponed with the increase in IPFs between the particles. In the fluidization stage, the upward gas flow can reach the bed surface, which indicates the bed reaches the spouting condition by applying the $\mathbf{Bo_g} = 5$. Under this condition, the gas flow crosses the bed by creating a channeling state. At the $\mathbf{Bo_g} = 50$, the required value of the gas velocity is insufficient to reach the bed surface, so it can be expected that more gas velocity is needed to achieve the spouting condition. These results shows that u_{ms} is postponed by increasing IPFs between the particles.

As the number of bubbles at the top of the bed increase, the number of massive agglomerates increases in the bottom of the bed due to the effect of the weight force of upper particles that are acting on the particles placed at the lower zones. However, the formation of massive agglomerates was postponed as the cohesive force decreased. By comparing the results, it can be seen that the expanded beds in the defluidization state (top images) is greater than that of the fluidization state (bottom images), which was consistent with our experimental observations.

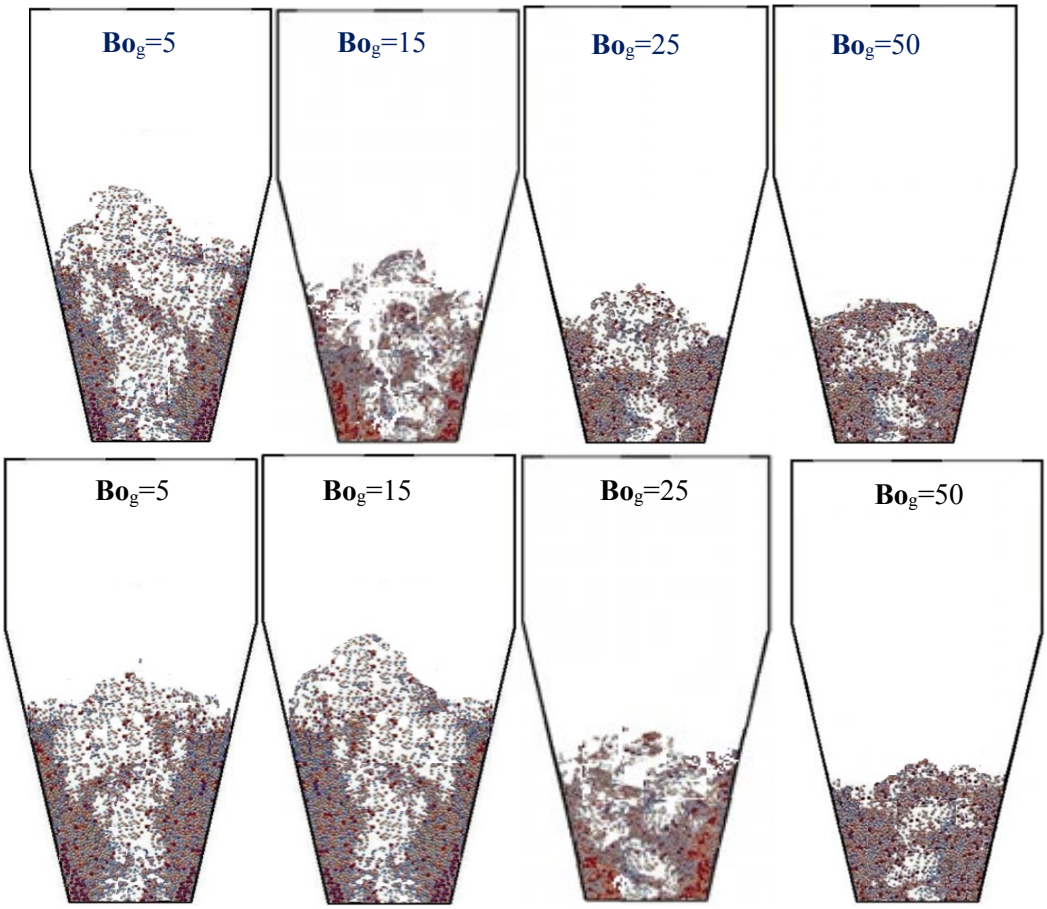

Figure 6. The contour plots of the solid volume fraction of fluidization (top images) and defluidization (bottom images) cycles for the simulated bed by applying different $\mathbf{Bo}_g$ values[u_g = 0.6 m/s, h_0 = 4.8 cm].

Figure 7 shows the results of the fluidization/defluidization curves of TiO_2 simple-agglomerates in a simulated bed by applying different $\mathbf{Bo}_g$ values of 5, 15, 25, and 50 at h_0 = 4.8 cm. As it can be seen, the normalized bed pressure drop and hysteresis phenomena in the pressure drop profile increase significantly by increasing $\mathbf{Bo}_g$, which is due to the high interactions between the cohesive particles. As $\mathbf{Bo}_g$ increases, u_{ms} decreases, while u_{mb} increases. Ye et al. [34] showed that the beds containing Group A particles represent $u_{mb}/u_{ms} > 1$, which indicates that ignoring the cohesion forces between particles leads to the deviation of simulation results from the experimental data. The phenomenon of pressure drop overshoot can be observed in the simulation results according to what is observed in the experiments. The value of pressure overshoot can be attributed to the particle-particle cohesive forces, and tangential forces between particles and the wall [14]. The magnitude of pressure overshoots expands by increasing the $\mathbf{Bo}_g$ value. However, considering a low value of cohesive force ($\mathbf{Bo}_g$ = 5), the pressure overshoot and the u_{ms} variation still exist for Geldart A particles. Tsinontides and Jackson [39] found that the pressure overshoot occurs through the beds of FCC particles that are categorized as Geldart group A. The CFD-DEM simulations with a low value of cohesion force ($\mathbf{Bo}_g$ = 5) showed a low-pressure overshoot, whereas considering cohesion ($\mathbf{Bo}_g$ = 50) it could be seen a distinct pressure overshoot. The magnitude of the cohesive force between the particles decreases by increasing the gas velocity as the bed expands.

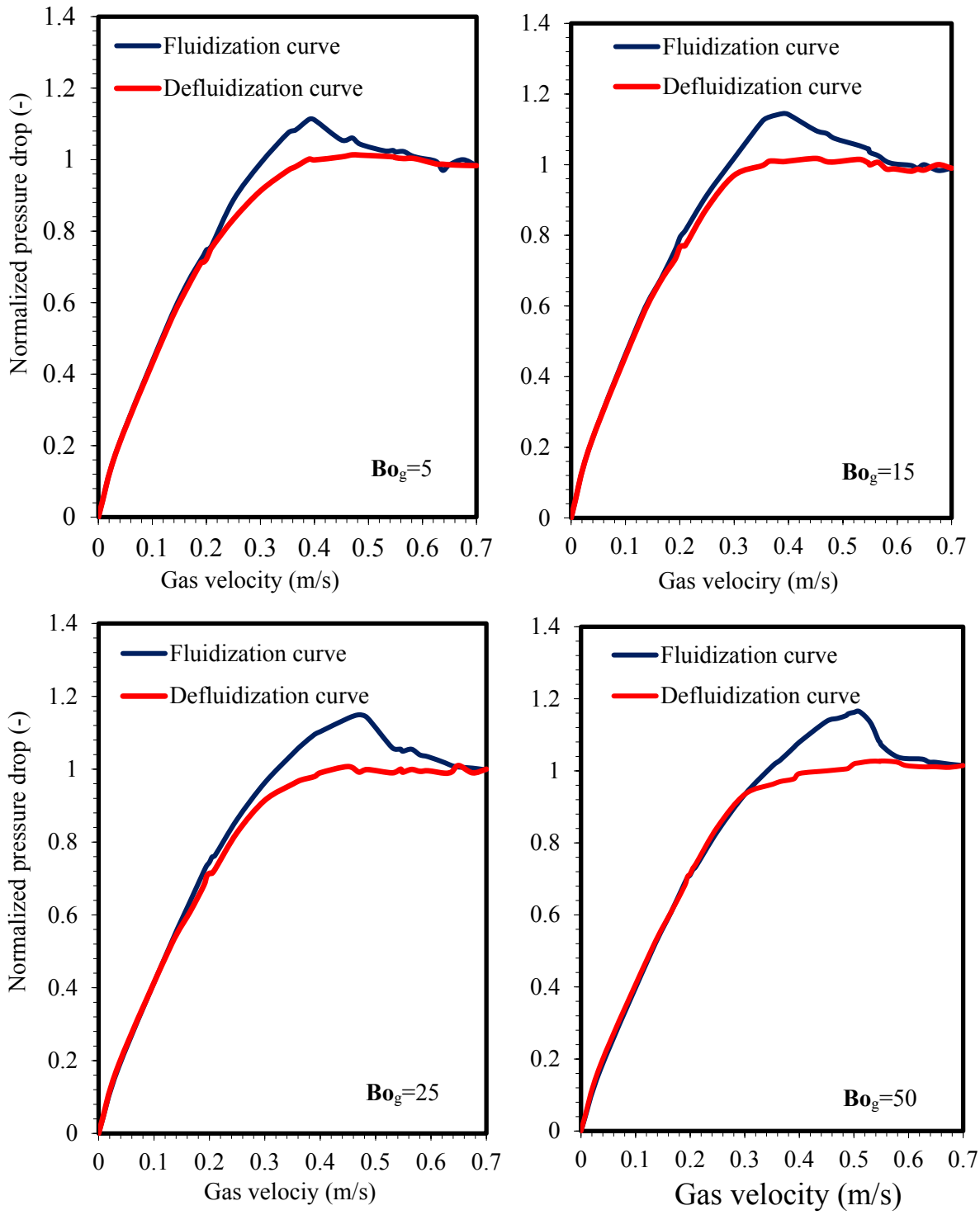

Figure 7. The fluidization/defluidization curves of TiO_2 simple-agglomerates in a simulated bed by applying different $\mathbf{Bo}_g$ values at h_0 = 2.4 cm.

4.2.2. Effect of the static bed height on IPF

Figure 8 shows the simulation results of normalized pressure drop profiles of the bed with h_0 values of 1.2, 2.4, 3.6, and 4.8 cm by considering the $\mathbf{Bo}_g$ value of 50 and Gaussian-type PSD. The results are presented in fluidization, and defluidization (b) curves. As it can be found, the normalized pressure drop decreases by decreasing h_0, which exhibits that the gas flow is hardly transferred from inside the deep beds, thus leading to an increase in u_{ms}. For Geldart A particles, the static bed

height affects the cohesive force between NPs. The results showed by using a low value of the $\mathbf{Bo}_g$ number, the normalized pressure drop is reduced compared with the results by applying a high value of the $\mathbf{Bo}_g$ number (Figure 7a), which indicates that the reduction of the adhesion effects between particles has led to the increased particle compaction, especially in the spout zone. An overestimated approximate in the value of u_{ms} was attributed to the physical characteristics of the bed, such as polydispersity, the initial static bed height, and the cohesion between simple-agglomerates and particles with the wall under the real conditions.

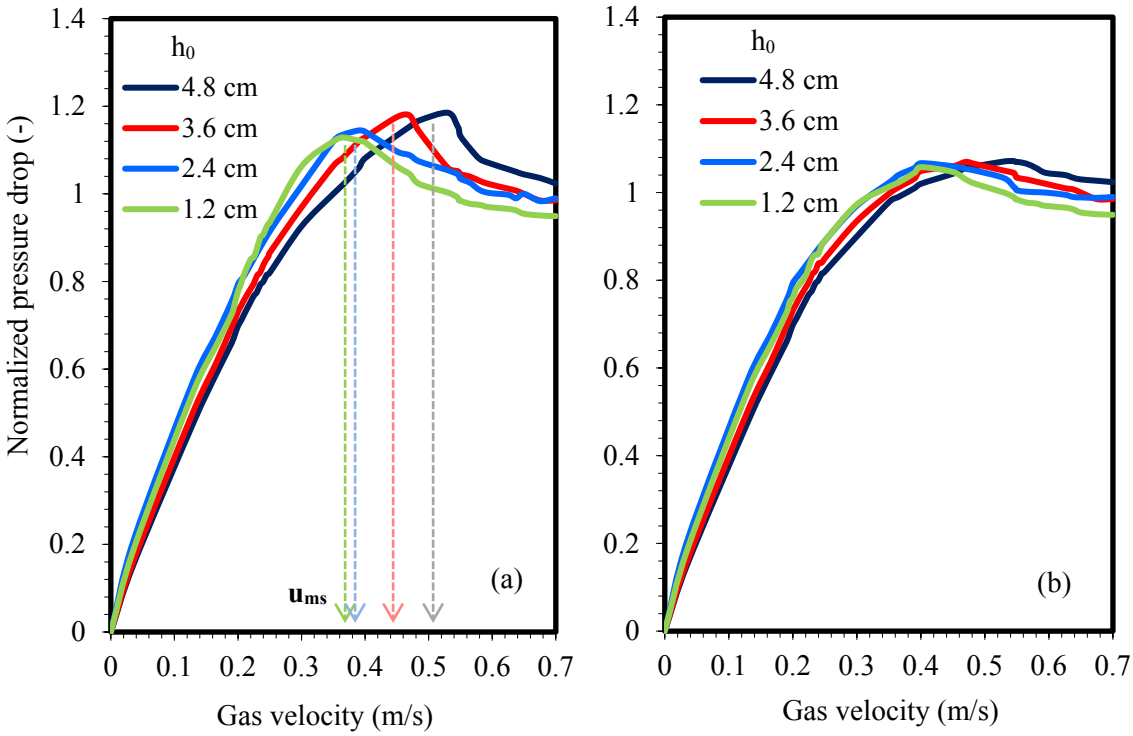

Figure 8. The simulation results of the normalized pressure drop profiles of the bed with h_0 values of 1.2, 2.4, 3.6, and 4.8 cm by considering the $\mathbf{Bo}_g$ value of 25 and Gaussian-type PSD [(a) fluidization, and (b) defluidization curves].

Table 7 shows the experimental data and simulation results for u_{ms} by applying different values of $\mathbf{Bo}_g$ for beds with various h_0 values. The mean relative error (MRE, %) between the experimental data and simulation results of u_{ms} are provided in this table within the brackets. As it can be found, the simulated values of u_{ms} for a low static bed height (h_0 = 1.2 cm) are more consistent with the experimental data. The highest deviation between the experimental data and simulation results are found at the h_0 = 4.8 cm, which indicates high agglomeration of NPs due to particle-particle collisions in the real state. In contrast, the lowest deviation between the experimental data and simulation results is found at the h_0 = 1.2 cm. In addition, using a $\mathbf{Bo}_g$ = 25 led to accurate simulation results and minimum deviation between the experimental and simulation results. At low particle loadings (i.e., h_0 = 1.2 cm), because of the dependency of β_i (Eq. 6) on ϕ_p^{-2} the main dissipation is due to the drag interaction between the gas and particles. In contrast, in the higher static bed heights (i.e., h_0 = 4.8 cm), the contribution of the weight force is more significant than that

of the drag force between particles. In addition, the tendency of NPs to agglomeration takes place at high $\mathbf{Bo}_g$ values. As it can be seen, the relative error values increase drastically with the increase in the $\mathbf{Bo}_g$ number at low h_0 values, while this impact is significantly lower at high h_0 values. This result indicates that the high impact of the IPF between the particles on the expected u_{ms} values was prominent at the fluidized bed with low h_0 values. Also, the effect of the $\mathbf{Bo}_g$ number on the predicted u_{ms} results was slightly more evident by increasing h_0.

Table 7
The experimental data and simulation results for the u_{ms} of the fluidized bed at different h_0 values.

h_0 (cm)	u_{ms} (m/s) [MRE, %]				
	Experimental	**Simulation (Bo_g = 5)**	**Simulation (Bo_g = 15)**	**Simulation (Bo_g = 25)**	**Simulation (Bo_g = 50)**
1.2	0.37	0.31 [-16.23]	0.34 [-8.12]	0.36 [-2.7]	0.42 [13.52]
2.4	0.42	0.35 [-16.66]	0.39 [-7.16]	0.40 [4.12]	0.48 [14.28]
3.6	0.50	0.37 [-26.00]	0.41 [-18.00]	0.51 [2.00]	0.57 [15.00]
4.8	0.55	0.40 [-27.27]	0.45 [-18.21]	0.52 [-5.45]	0.64 [16.36]

4.2.3. Effect of PSD

Figure 9 shows the contour plots of the solid volume fraction of fluidization (top images) and defluidization (bottom images) cycles for the simulated bed with the h_0 value of 4.8 cm and the u_g value of 0.6 m/s, by considering two PSD types of Gaussian and narrow-cut. A constant $\mathbf{Bo}_g$ value of 15 was selected in the simulations. As it can be found, the highest values of the solid volume fraction in the bed were found in the annular zone, while the lowest values were found in the spout zone at the center of the bed. In addition, the expanded height of the beds with the PSD types of narrow-cut and Gaussian were close to each other. The simulation results showed that the bed with narrow-cut type PSD has a hydrodynamic behavior similar to that of spouting and slugging regimes, while the fluidization quality of the bed improves by the existance of fine particles that act as the lubricant [40]. The hydrodynamic behavior of the bed with Gaussian-type PSD is similar to that of the bed with narrow-cut type PSD, although the size of slugs formed in the bed with Gaussian-type PSD is lager than that of the same in the narrow-cut type PSD. By comparing the results, it can be seen that the hydrodynamic behavior of the simulated bed with Gaussian-type PSD is more similar to that of experimental observations. The presence of large slugs in the bed under real conditions is a function of the cohesive force between the NPs, which leads to trapping and increasing air bubbles within the bed [41]. As a result, for further studies, the conditions of the simulation bed are considered as Gaussian-type PSD.

The results also indicate an excellent particle mixing in the bed because of the wide PSD of simple-agglomerates. Thus, a more homogeneous bed expansion occurs in the bed with Gaussian-type PSD than in the bed with narrow-cut type PSD. However, the value of superficial gas velocity lies between u_{ms} and u_{mb} ($1.1u_{ms}$), which confirms the uniform combination of fine and coarse particles in the

bed with Gaussian-type PSD. In contrast, the fluidization behavior of the bed with narrow-cut type PSD slightly tends to heterogeneous fluidization, and the bed expansion at the $u_{mb} > u_{ms}$ is attributed to the segregation of large particles from the fine particles, where more coarse particles transfer to the bottom of the bed and highly cohesive fine ones remain at the top and near the walls of the bed. This behavior is explained by considering the nature of the packed bed, where smaller particles can fill some of the voids formed by coarser particles and lead to a decrease in the void fraction of the bed [37]. However, these qualitative differences in the fluidization behavior of particles with particle size of 45-100 μm cannot be seen in the simulation results of beds by considering Gaussian-type or narrow-cut type PSD.

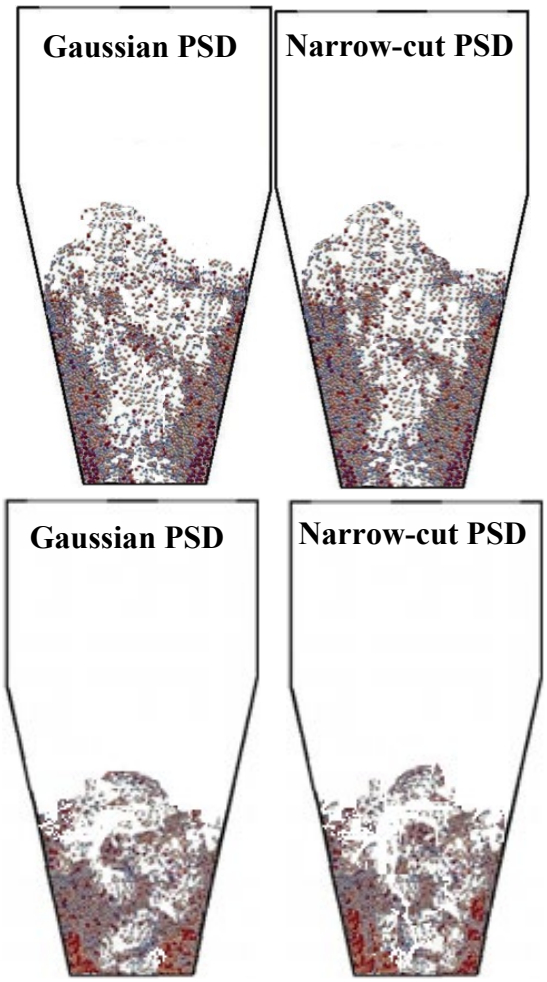

Figure 9. The contour plots of solid volume fraction of fluidization (top images) and defluidization (bottom images) cycles for the simulated bed with the PSD types of Gaussian and narrow-cut [h_0 = 4.8 cm, u_g = 0.6 m/s, $\mathbf{Bo}_g$ = 25].

Figure 10 shows the simulation results of fluidization/defluidization curves of TiO_2 simple-agglomerates in a simulated bed with the h_0 value of 2.4 cm by considering the $\mathbf{Bo}_g$ value of 25 for two PSD types of Gaussian and narrow-cut. The results showed that the u_{ms} of the bed with narrow-cut type PSD was slightly higher than the same with the Gaussian-type PSD, while a reverse trend was found in the case of u_{mb}. As it can be seen, the u_{ms} values of

the beds with narrow-cut and Gaussian-type PSD were 0.45, and 0.40 m/s respectively, whereas their corresponding u_{mb} values were 0.49, and 0.46 m/s respectively. A higher value of the u_{ms} of the bed represents the lower tendency in simple-agglomerates for segregation. This result indicates that the u_{ms} value of the bed with narrow-cut type PSD type is slightly higher than that of the bed with Gaussian PSD type. This finding disagreed with the results obtained from the conventional fluidized bed [5, 14, 21, 40]. Gauthier et al. [21] presented that the choice of the PSD types of Gaussian and narrow-cut led to the same u_{mf} value in the fluidized bed. The most important reason for an increase in the value of the u_{ms} of the bed with narrow-cut type PSD is the normally fine particles filling the voids between the coars ones. The presence of fine particles (d_p = 30 μm) along with coarse particles (d_p = 90 μm) provides a smoother fluidization associated with and better gas-solid contact, which lead to a reduction in the value of u_{ms} in the bed with Gaussian-type PSD. Fine particles can more easily slip in the voids between coarser simple-agglomerates because of the lubricant effect, which reduce the friction forces between the particles and reduce the u_{ms} value.

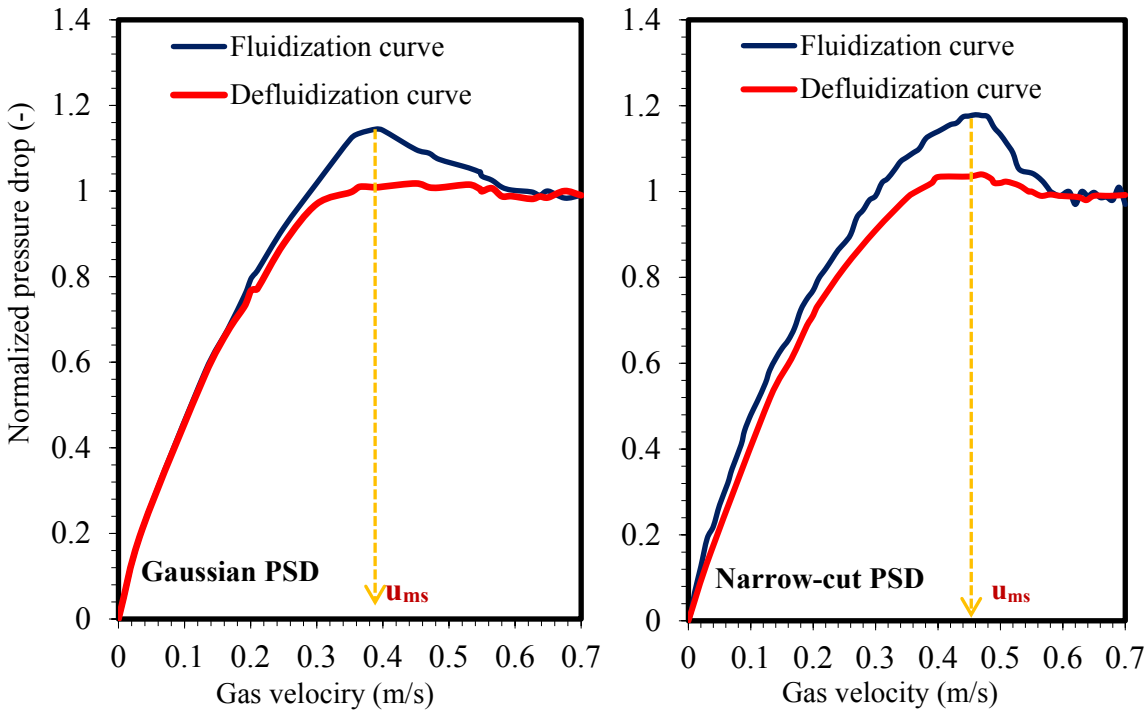

Figure 10. The Fluidization/defluidization curves of TiO_2 simple-agglomerates in a simulated bed with the h_0 value of 2.4 cm by considering two PSD types of Gaussian and narrow-cut.

Table 8 shows the u_{ms} values of the simulated bed with different h_0 values by considering two PSD types of Gaussian, and narrow-cut. The mean relative error (MRE, %) between the experimental data and simulation results of u_{ms} are provided in this table within the brackets. As it can be found, the u_{ms} values with wide PSDs were lower than the u_{ms} values for narrow-cut type PSD with the same average diameter. The value of u_{ms} in the case of Gaussian-type PSD showed less deviations than that the narrow-cut type PSD. As it can be seen, by increasing the h_0 value, the MRE % between the experimental data and simulation

results increases, which exhibits that selecting any PSD and $\mathbf{Bo}_g$ value affects the results of when selecting the bed with high hights of particles more than that in case of the beds with low loadings of particles. The most important reason for this can be considered the formation of large slugs in the bed with higher static bed heights, which will lead to the discrepancy between the results [20, 41].

The biggests discrepancy between the experimental data and simulation results in the case of Gaussian-type PSD is achieved at the lower static bed height . In contrast, the biggest discrepancy between the experimental data and simulation results in the case of narrow-cut type PSD is obtained at higher static bed height. However, the uncertainty about experimental data in the bed with more particle loading is also high, affecting the relative error results. The result indicates a high impact of selecting the PSD of the conical fluidized bed on the predicted u_{ms} values. In addition, the effect of the bed PSD on the predicted values of u_{ms} considerably increases by increasing the h_0 value.

Table 8

The u_{ms} and mean relative error (%) values of the experimental data and simulation results for u_{ms} by considering two PSD types of Gaussian and narrow-cut.

h_0 (cm)	u_{ms} (m/s) [MRE, %]	
	Simulation (Gaussian PSD)	**Simulation (Narrow-cut PSD)**
1.2	0.36 [-2.70]	0.39 [4.52]
2.4	0.40 [-4.12]	0.45 [6.46]
3.6	0.51 [-2.00]	0.54 [8.00]
4.8	0.52 [-5.46]	0.59 [9.09]

4. Conclusions

This study provided experimental data and simulation results to understand the effect of static bed height on the minimum spouting velocity (u_{ms}) of the polydispersed TiO_2 simple-agglomerates in a conical fluidized bed. The experiments were carried out in the bed containing particles with the diameters in the range of 30-90 μm belonging to the A group of Geldart's classification. The effects of PSD and interparticle force (IPF) on the predicted u_{ms} results and hysteresis in the bed pressure drop were studied by an approach having coupled computational fluid dynamics and discrete element method (CFD-DEM). Two systems, including the PSD types of Gaussian and narrow-cut, were examined through fluidization and defluidizations stages. The results showed that the normalized bed pressure drop increased significantly by increasing the $\mathbf{Bo}_g$ value, and hysteresis in the pressure drop curves was evident, which was justified by the interaction between simple-agglomerates. As the $\mathbf{Bo}_g$ value increases, the u_{ms} value decreases, while the u_{mb} value also increases. In addition, by changing the $\mathbf{Bo}_g$ value from 5 to 15, a minor change was observed in the pressure overshoot. As the PSD changes from narrow-cut type to Gaussian-type , the u_{ms} value decreases, while the u_{mb} increases. The results showed that choosing the bed with Gaussian-type PSD led to more accurately predicting the u_{ms} value than choosing the beds with the narrow-cut type PSD. The impact of IPF on the expected u_{ms} value became more critical because of an increase in static bed heights. The least discrepancy between the experimental data

and simulation outputs was obtained in the bed with Gaussian-type PSD and less static bed heights . The relative error analysis outcomes showed the predicted u_{ms} results affected at a low static bed height (h_0 = 1.2 cm) were: IPF > PSD-type. In contrast, for the high static bed height (h_0 = 4.8 cm) they were: PSD-type > IPF. As it can be concluded for the powder A type, the type of PSD has a significant effect on predicting the results of u_{ms}. Excellent results were obtained for the polydispersed bed by considering Gaussian-type PSD.

Acknowledgement

The author whould like to thank Hamedan University of Technology for their support.

References

[1] Tanfara, H., Pugsley, T. and Winters, C., "Effect of particle size distribution on local voidage in a bench-scale conical fluidized bed dryer", *Dry. Technol.*, **20** (6), 1273 (2002).

[2] Das, H. J., Mahanta, P., Saikia, R. and Aamir, M. Sh., "Performance evaluation of drying characteristics in conical bubbling fluidized bed dryer", *Powder Technol.*, **374** (1), 534 (2020).

[3] Foroughi-Dahr, M., Sotudeh-Gharebagh, R. and Mostoufi, N., "Characterization of flow properties of pharmaceutical pellets in draft tube conical spout-fluid beds", *J. Ind. Eng. Chem.*, **68** (1), 274 (2018).

[4] Agu, C. E., Pfeifer, Ch. and Moldestad, B. M. E., "Prediction of void fraction and minimum fluidization velocity of a binary mixture of particles: Bed material and fuel particles", *Powder Technol.*, **349** (1), 107 (2019).

[5] Sun, G. L. and Grace, J. R., "Effect of particle-size distribution in different fluidization regimes", *AIChE J.*, **38** (1), 722 (1992).

[6] Yang, W. -Ch., Handbook of fluidization and fluid-particle systems, 1st ed., CRC Press, (2003).

[7] Zhong, W., Chen, X. and Zhang, M., "Hydrodynamic characteristics of spout-fluid bed: Pressure drop and minimum spouting/spout-fluidizing velocity", *Chem. Eng. J.*, **118** (1-2), 37 (2006).

[8] Ma, J., van Ommen, J. R., Liu, D., Mudde, R. F., Chen, X., Wagner, E. C. and Liang, C., "Fluidization dynamics of cohesive Geldart B particles, Part I: X-ray tomography analysis", *Chem. Eng. J.*, **359** (1), 1024 (2019).

[9] Shabanian, J. and Chaouki, J., "Local characterization of a gas-solid fluidized bed in the presence of thermally induced interparticle forces", *Chem. Eng. Sci.*, **119** (1), 261 (2014).

[10] Wang, X. S., Rahman, F. and Rhodes, M. J., "Nanoparticle fluidization and Geldart's classification", *Chem. Eng. Sci.*, **62** (1), 3455 (2007).

[11] Wormsbecker, M., van Ommen, R., Nijenhuis, J., Tanfara, H. and Pugsley, T., "The influence of vessel geometry on fluidized bed dryer hydrodynamics", *Powder Technol.*, **194** (1), 115 (2009).

[12] Bahramian, A. R., "The mutual effects between the interparticle forces and mechanical properties on fluidization of TiO_2 nanoparticle agglomerates in a conical fluidized bed: nanoindentation and pressure fluctuation analysis", *J. Nanopart. Res.*, **21** (1), 196 (2019).

[13] Castellanos, A., Valverde, J. M. and Quintanilla, M. A. S., "Agglomeration and sedimentation in gas-fluidized beds of cohesive powders", *Phys. Rev. E*, **64** (1), 041304 (2001).

[14] Bahramian, A. R. and Olazar, M.,

"Fluidization of micronic particles in a conical fluidized bed: Experimental and numerical study of static bed height effect", *AIChE J.*, **58** (1), 730 (2012).

[15] Jiliang, M., Xiaoping, Ch. and Daoyin, L., "Minimum fluidization velocity of particles with wide size distribution at high temperatures", *Powder Technol.*, **235** (1), 271 (2013).

[16] Rao, A., Curtis, J. S., Hancock, B. C. and Wassgren, C., "The effect of column diameter and bed height on minimum fluidization velocity", *AIChE J.*, **56** (1), 2304 (2010).

[17] Liu, D., van Wachem, B. G. M., Mudde, R. F., Chen, X. and van Ommen, J. R., "An adhesive CFD-DEM model for simulating nanoparticle agglomerate fluidization", *AIChE J.*, **62** (1), 2259 (2016).

[18] Shabanian, J., Fotovat, F., Chaouki, J. and Bouffard, J., "Fluidization behavior in a gas-solid fluidized bed with thermally induced inter-particle forces", Proceedings of *10th International Conference on Circulating Fluidized Beds and Fluidization Technology*, Sun River, Oregon, USA, (2011).

[19] Bahramian, A. R. and Olazar, M., "Evaluation of elastic and inelastic contact forces in the flow regimes of Titania nanoparticle agglomerates in a bench-scale conical fluidized bed: A comparative study of CFD-DEM simulation and experimental data", *Chem. Eng. Res. Des.*, **176** (1), 34 (2021).

[20] Feng, R., Li, J., Cheng, Zh., and Fang, Y., "Influence of particle size distribution on minimum fluidization velocity and bed expansion at elevated pressure", *Powder Technol.*, **320** (1), 27 (2017).

[21] Gauthier, D., Zerguerras, S. and Flamant, G., "Influence of the particle size distribution of powders on the velocities of minimum and complete fluidization", *J. Chem. Eng. Japan*, **74** (1), 181 (1999).

[22] Tsuji, T., Yabumoto, K. and Tanaka, T., "Spontaneous structures in three-dimensional bubbling gas-fluidized bed by parallel DEM–CFD coupling simulation", *Powder Technol.*, **184** (1), 132 (2008).

[23] Yang, S., Luo, K., Fang, M., Fan, J. and Cen, K., "Influences of operating parameters on the hydrodynamics of a 3-D spout-fluid bed based on DEM modelling approach", *Chem. Eng. J.*, **247** (1), 161 (2014).

[24] Xu, Y., Li, T., Musser, J., Liu, X., Xu, G. and Rogers W. A., "CFD-DEM modeling the effect of column size and bed height on minimum fluidization velocity in micro fluidized beds with Geldart B particles", *Powder Technol.*, **318** (1), 321 (2017).

[25] Groger, U., and Heyes, M., "Modelling and measuring of cohesion in wet granular materials", *Powder Technol.*, **133** (1-3), 203 (2003).

[26] Fan, X. and Zhou, Ch., "Estimation of bed expansion and separation density of gas-solid separation fluidized beds using a micron-sized-particle-dense medium", *Separations*, **8** (242),1 (2021).

[27] Liu, P., LaMarche, C. Q., Kellogg, K. M. and Hrenya, Ch. M., "Fine-particle defluidization: Interaction between cohesion, Young's modulus and static bed height", *Chem. Eng. Sci.*, **145** (1), 266 (2016).

[28] Galvin, J. E. and Benyahia, S., "The effect of cohesive forces on the fluidization of aeratable powders", *AIChE J.*, **60** (1), 473 (2014).

[29] Bahramian, A. R., Olazar, M. and

Ahmadi, G., "Effect of slip boundary conditions on the simulation of micro-particle velocity fields in a conical fluidized bed", *AIChE J.*, **59** (1), 4502 (2013).

[30] McKeen, T. and Pugsley, T., "Simulation and experimental validation of a freely bubbling bed of FCC catalyst", *Powder Technol.*, **129** (1), 139 (2003).

[31] Endresa, S. Ch., Ciacchi, L. C. and Mädler, L., "A review of contact force models between nanoparticles in agglomerates, aggregates, and films", *J. Aerosol Sci.*, **153** (1), 105719 (2021).

[32] Castellanos, A., "The relationship between attractive interparticle forces and bulk behaviour in dry and uncharged fine powders", *Adv Phys.*, **54** (4), 263 (2005).

[33] Visser, J., "An invited review: van der Waals and other cohesive forces affecting powder fluidization", *Powder Technol.*, **58** (1), 1 (1989).

[34] Ye, M., van der Hoef, M. A. and Kuipers, J. A. M., "The effects of particle and gas properties on the fluidization of Geldart A particles", *Chem. Eng. Sci.*, **60** (16), 4567 (2005).

[35] Kobayashi, T., Tanaka, T., Shimada, N. and Kawaguchi, T., "DEM-CFD analysis of fluidization behavior of Geldart Group A particles using a dynamic adhesion force model", *Powder Technol.*, **248** (1), 143 (2013).

[36] Dong, Y., Perez, D., Voter, A. F. and Martini, A., "The roles of statics and dynamics in determining transitions between atomic friction regimes", *Tribology Let.*, **42** (1), 99 (2011).

[37] Cundall, P. A. and Strack, O. D. L., "A discrete numerical model for granular assemblies", *Geotech. Geol.*, **29** (1), 47 (1979).

[38] Galvin, J. E. and Benyahia, S., "The effect of cohesive forces on the fluidization of aeratable powders", *AIChE J.*, **60** (1), 473 (2014).

[39] Tsinontides, S. C. and Jackson, R., "The mechanics of gas-fluidized beds with an interval of stable fluidization", *J. Fluid Mech.*, **255** (1), 237 (1993).

[40] Grace, J. R. and Sun, G., "Influence of particle-size distribution on the performance of fluidized-bed reactors", *Can. J. Chem. Eng.*, **69** (1), 1126 (1991).

[41] Peng, Z., Doroodchi, E., Luo, C. and Moghtaderi, B., "Influence of void fraction calculation on fidelity of CFD-DEM simulation of gas-solid bubbling fluidized beds", *AlChE J.*, **60** (1), 2000 (2014).